Materials Today Bio 32 (2025) 101913

Contents lists available at ScienceDirect

Materials Today Bio

journal homepage: www.journals.elsevier.com/materials-today-bio

A glutathione-responsive ferroptotic inducer with elevated labile iron pool and self-supplied peroxide for chemodynamic therapy

Penghui Wei [a,b,c,1], Xuegang Niu [a,b,c,1], Dengliang Wang [a,b,c,*,1], Chengzhong Du [a,b,c], Mingtao Zhu [a,d], Hongjia Zheng [a,b,c], Yongrui Hu [a,b,c], Yu Tian [a,b,c], Wei Huang [a,b,c], Chengyu Ding [a,b,c], Yuanxiang Lin [a,b,c], Yang Zhu [a,b,c,**], Dezhi Kang [a,b,c,***]

[a] Department of Neurosurgery, The First Affiliated Hospital, Fujian Medical University, Fuzhou, 35005, China
[b] Department of Neurosurgery, National Regional Medical Center, Binhai Campus of First Affiliated Hospital, Fujian Medical University, Fuzhou, 350212, China
[c] Fujian Provincial Institutes of Brain Disorders and Brain Sciences, The First Affiliated Hospital, Fujian Medical University, Fuzhou, 35005, China
[d] Department of Neurosurgery, Xiamen Xinglin Hospital (Xiamen Infectious Disease Hospital), Xiamen, 361000, China

ARTICLE INFO

Keywords:
Chemodynamic therapy
Ferritin heavy chain
Labile iron pool
O-GlcNAcylation
Ferroptosis

ABSTRACT

Chemodynamic therapy (CDT) is a novel approach in the treatment of tumors in which ferrous iron (Fe^{2+}) is the primary catalyst of the Fenton reaction. However, Fe^{2+} is typically stored in an oxidized mineral form as ferric iron (Fe^{3+}) in ferritin, significantly limiting the efficacy of CDT. This work describes the preparation of redox-responsive nanoparticles (MO@DSSP NPs) embedded with OSMI-1 and methyl linoleate hydroperoxide (MLH) to synergistically enhance CDT efficacy, optimize peroxide supply and deplete glutathione (GSH). The redox-responsive MO@DSSP NPs undergo disintegration after being internalized by tumor cells due to the reductive tumor microenvironment, consuming GSH while releasing OSMI-1 and MLH. This process increases the intracellular labile iron pool (LIP) and oxidative stress at the tumor site by inhibiting O-GlcNAcylation of ferritin heavy chain (FTH). Furthermore, obstructing O-GlcNAc modification triggers mitochondrial fragmentation alongside autophagy, thus contributing an extra source of reactive iron. The increased LIP significantly promotes the generation of hydroxyl radical (·OH) that causes lipid peroxidation, consequent damage of the cell membrane and ferroptosis. Therefore, this study describes an attractive CDT nanoagent that effectively inhibits the O-GlcNAcylation of FTH to mobilize endogenous Fenton-type metals, as well as offers a basis to the exploration of LIP-activatable MLH with high CDT efficacy, demonstrating significant potential for clinical applications.

1. Introduction

Chemodynamic therapy (CDT) has gained attention as a novel approach in tumor-targeted therapy that primarily triggers Fenton reactions or Fenton-like reactions to produce cytotoxic ·OH in the tumor microenvironment (TME), thereby enabling a precise and targeted killing of tumor cells [1–5]. The toxic reactive oxygen species (ROS) produced by Fenton-type reactions are not dependent on either molecular oxygen (O_2) or an external ultrasound source [6], allowing CDT to circumvent the main limitations of sonodynamic therapy, in which ROS formation is strongly inhibited by the hypoxic TME [7–11]. However, the therapeutic efficacy of CDT remains far from desirable despite its promising potential. Indeed, its therapeutic efficacy is significantly limited by the presence of endogenous hydrogen peroxide (H_2O_2), free Fe^{2+}, and high levels of reductive GSH in the TME [12–17].

Although transition metals such as Fe, manganese (Mn), and copper (Cu) can effectively produce ·OH and deplete GSH by participating in Fenton reactions, the main concern with this approach is that the overuse of exogenous Fenton - related metals in treatment could lead to potential side effects, manifesting as both acute and chronic toxicities [18–23]. Therefore, the exploration of alternative strategies to increase the effectiveness of CDT is very attractive. Fe is a crucial transition metal

* Corresponding author. Department of Neurosurgery, The First Affiliated Hospital, Fujian Medical University, Fuzhou, 35005, China.
** Corresponding author. Department of Neurosurgery, The First Affiliated Hospital, Fujian Medical University, Fuzhou, 35005, China.
*** Corresponding author. Department of Neurosurgery, The First Affiliated Hospital, Fujian Medical University, Fuzhou, 35005, China.
E-mail addresses: wdlchina2003@sina.cn (D. Wang), zhuyang@mail.ustc.edu.cn (Y. Zhu), kangdezhi@fjmu.edu.cn (D. Kang).
[1] These authors contributed equally to this work.

https://doi.org/10.1016/j.mtbio.2025.101913
Received 20 March 2025; Received in revised form 22 May 2025; Accepted 26 May 2025
Available online 29 May 2025

in biological systems [24–27]. A small fraction of intracellular Fe^{2+}, either free or weakly bound and referred to as the labile iron pool (LIP), is redox-active and can initiate Fenton-type reactions within cells [28–32]. The storage and release of Fe^{2+} in cells are tightly regulated by ferritin, thereby limiting the Fe-regulated Fenton reaction and subsequently preventing oxidative damage under normal conditions [33–37]. Moreover, tumor cells overexpress FTH, a ferroxidase enzyme that significantly reduces the therapeutic effect of CDT [38–40]. Importantly, the O-GlcNAcylation of FTH at serine 179 impairs its interaction with NCOA4, thereby suppressing ferritinophagy. Inhibition of this modification by OSMI-1 restores the FTH–NCOA4 interaction and promotes ferritin degradation [41]. Moreover, suppression of O-GlcNAcylation also triggers mitochondrial fragmentation and mitophagy, leading to the release of labile iron, which collectively enhances the sensitivity of tumor cells to ferroptosis [42–45]. From this perspective, the reduction of O-GlcNAc modification of ferritin significantly triggers both ferritinophagy and mitophagy, increasing intracellular LIP levels and ensuring a sufficient supply of labile iron to start the Fenton reaction, thereby improving CDT mediated by lipid peroxidation (LPO) [46]. However, no progress has been made in the inhibition of O-GlcNAcylation of FTH to amplify CDT-mediated ferroptosis.

This work describes the development of a GSH-responsive chemodynamic nanoagent (MO@DSSP NPs) designed to inhibit O-GlcNAcylation of FTH, and regulates labile iron and releases methyl linoleate hydroperoxide (MLH) in situ, thereby enhancing LIP-mediated CDT efficacy (Scheme 1). MO@DSSP NPs are fabricated by nanoprecipitation using GSH-responsive DSPE-S-S-PEG, the O-GlcNAcylation inhibitor OSMI-1, and MLH. Once the MO@DSSP NPs are internalized, the endogenous overproduction of GSH cleaves disulfide bonds, which in turn result in the co-release of the O-GlcNAcylation inhibitor OSMI-1 and MLH at the tumor site. This approach not only improves targeting and depleted GSH but also reduces side effects on normal tissues, resulting in improved safety and selectivity. Specifically, OSMI-1 effectively induces ferritin and mitochondrial autophagy, thus promoting the accumulation of intracellular LIP, amplifying the Fenton reaction. Moreover, the MLH released by the cleavage of the disulfide bond provides a sufficient supply of hydroperoxides, further enhancing Fenton reaction in situ and significantly improving CDT efficacy. Both in vitro and in vivo experiments demonstrated that MO@DSSP NPs attained a self-sustained supply of LIP and hydroperoxides, resulting in an excellent catalytic performance in the Fenton reaction and impressive reduction of GSH. This enhanced the sensitivity of tumor cells to oxidative stress and irreversible ferroptosis, thereby improving the therapeutic effect. This CDT enhancement strategy, combining Fe^{2+} and peroxide self-supply with GSH depletion, successfully overcomes the limitations of the tumor microenvironment, providing an effective approach to tumor therapy while reducing toxicity and metabolic burden.

2. Experimental section

2.1. •OH generation by MO@DSSP NPs-mediated catalytic reaction

To evaluate the catalytic generation of hydroxyl radicals (•OH) by MO@DSSP nanoparticles (NPs), a series of colorimetric assays were conducted using 3,3′,5,5′-tetramethylbenzidine (TMB) as the indicator. Briefly, MO@DSSP NPs were dispersed in aqueous solutions of TMB at a concentration of 40 μg/mL. The concentrations of MO@DSSP NPs ranged from 10 to 80 μg/mL. The reactions were performed under varying pH conditions to examine pH-dependent activity. Subsequently, $FeCl_2$ was added at a final concentration of 40 μg/mL to initiate Fenton-like catalytic reactions, and the mixtures were incubated at room temperature for 10 min. After incubation, the samples were centrifuged at 6000 rpm for 5 min to remove any particulate matter. The absorbance of the supernatant was measured at 652 nm using a UV–Vis spectrophotometer. To further confirm the generation of hydroxyl radicals, electron spin resonance (ESR) spectroscopy was performed using DMPO as a spin trapping agent.

2.2. Uptake and lysosomes colocalization

To investigate the cellular uptake and subcellular localization of

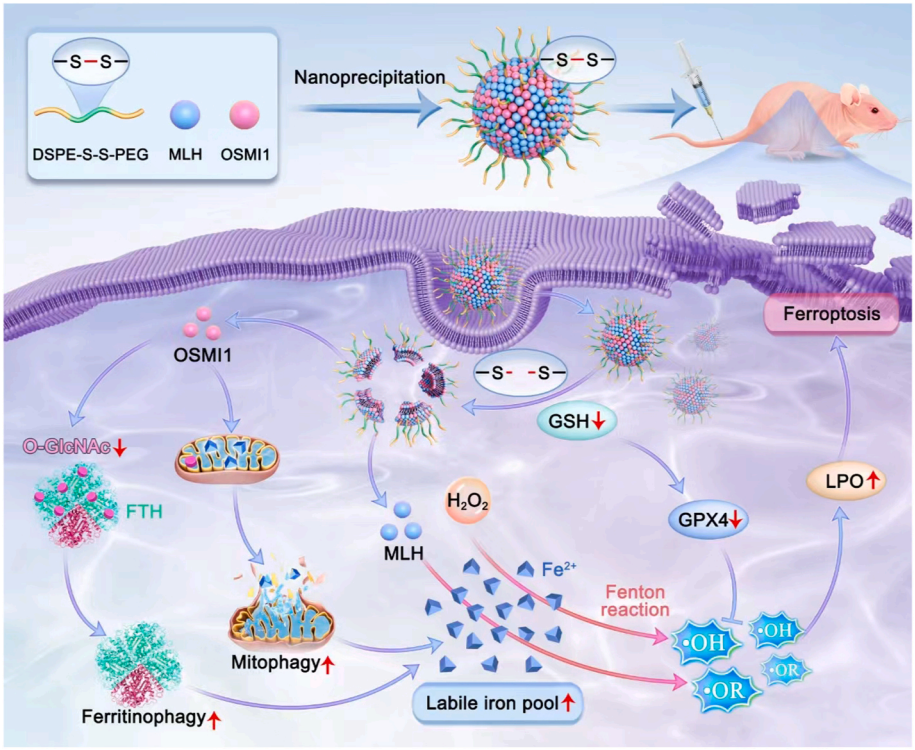

Scheme 1. Schematic illustration of the synthesis of MO@DSSP NPs and their antitumor mechanism.

MO@DSSP NPs, cells were incubated with Cy5-labeled MO@DSSP NPs for various time points: 30 min, 1 h, 2 h, and 4 h. After incubation, the cells were washed three times with PBS to remove unbound nanoparticles. For colocalization analysis, a dual-fluorescence staining protocol was applied. Cell nuclei were stained with Hoechst 33342 and lysosomes were labeled with LysoTracker Green, both incubated in the dark at 37 °C for 20 min. Following staining, the cells were washed with PBS to remove excess dye. High-resolution fluorescence images were acquired using a confocal laser scanning microscope (Zeiss LSM 800).

2.3. Cytotoxicity and cell apoptosis assessments

To assess the cytotoxicity of MO@DSSP NPs, U87MG human glioblastoma cells were seeded in 96-well plates at a density of 5×10^4 cells/well and allowed to adhere for 12 h. The cells were then treated with various concentrations of MO@DSSP NPs and incubated for 24 h. Subsequently, the culture medium was replaced with fresh medium containing 10 μL of Cell Counting Kit-8, and the cells were incubated for an additional 2 h at 37 °C. The absorbance at 450 nm was recorded using a microplate reader (model, manufacturer) to evaluate cell viability.

For fluorescence-based apoptosis and viability imaging, U87MG cells were seeded in glass-bottom confocal dishes and incubated for 24 h. Cells were then exposed to MO@DSSP NPs under the same concentration conditions for another 24 h. After treatment, cells were washed with PBS and stained with fluorescein diacetate (FDA, 5 μM) and propidium iodide (PI, 20 μM) for 20 min in the dark at 37 °C. The stained cells were imaged using a confocal laser scanning microscope.

2.4. In vitro ROS generation

To evaluate intracellular ROS generation, U87MG cells were seeded in culture dishes and incubated overnight to allow adherence. Cells were then treated with various formulations for 4 h under standard culture conditions. Following treatment, the cells were incubated with DCFH-DA and Hoechst 33342 for 20 min at 37 °C in the dark. After staining, the cells were washed thoroughly with PBS to remove excess dye, and fluorescence imaging was performed using CLSM. ROS fluorescence intensity was qualitatively observed and optionally analyzed using ImageJ for semiquantitative assessment.

2.5. Intracellular GSH and GSSG content

To evaluate the redox status of cells following treatment, intracellular levels of reduced glutathione (GSH) and oxidized glutathione (GSSG) were quantified. U87MG cells were seeded in 6-well plates at a density of 1×10^6 cells/well and allowed to adhere for 24 h. Cells were then treated with various formulations for an additional 24 h. After treatment, GSH and GSSG contents were measured according to the manufacturer's instructions (Total Glutathione (T-GSH)/Oxidized Glutathione (GSSG) Colorimetric Assay Kit and Elabscience). Absorbance was recorded at 412 nm using a microplate reader.

2.6. Analysis of the change of mitochondrial membrane potential

To assess changes in mitochondrial membrane potential, U87MG cells were seeded in confocal dishes and allowed to adhere overnight. Cells were then treated with different formulations for 24 h under standard culture conditions. Following treatment, the cells were washed with PBS and stained with JC-1 dye at 37 °C for 20 min in the dark, according to the manufacturer's protocol. After staining, cells were rinsed twice with PBS to remove excess dye. Fluorescence images were acquired using CLSM.

2.7. Hematological, biochemical analysis and histological staining

To evaluate the systemic effects of drug intervention, blood samples were collected from the retroorbital venous plexus before various formulations administration (day 0) and on days 1, 7, and 14. These samples were used for routine hematological and biochemical analyses. After 14 days of drug intervention, the mice were euthanized by cervical dislocation, and tissues from the heart, liver, spleen, lungs, and kidneys were collected for further analysis.

2.8. In vivo imaging

To evaluate the biodistribution of the nanoparticles, in vivo fluorescence imaging was performed using U87MG tumor-bearing nude mice. When tumors reached a volume of approximately 100–150 mm^3, the mice were intravenously injected with various formulations via the tail vein. Fluorescence images were captured at predetermined time points (1, 2, 4, 6, 8, 12, and 24 h post-injection) using an in vivo imaging system (IVIS Spectrum, PerkinElmer). During imaging, mice were anesthetized using isoflurane (2 % in oxygen) and placed in the imaging chamber.

2.9. In vivo chemodynamic efficacy

Animal experiments were conducted in line with the protocol sanctioned by The Ethical Committee of Fujian Medical University. U87MG cells were subcutaneously implanted into the right hind legs of all mice. The tumor-bearing mice were utilized for antitumor treatment once the tumor volume approximated 100 mm^3. U87MG tumor - bearing nude mice were arbitrarily allocated into four groups (with 5 mice in each group), and 10 mg/kg various formulations were intravenously administered to them. The tumor volumes as well as the body weights were documented every two days. Following 14 days of treatment, the mice were sacrificed for histological inspection.

3. Results and discussion

3.1. Fabrication and characterization of MO@DSSP NPs

MO@DSSP NPs were synthesized by nanoprecipitation using GSH-responsive DSPE-S-S-PEG, the O-GlcNAcylation inhibitor OSMI-1, and MLH. Transmission electron microscopy (TEM) images revealed that MO@DSSP NPs were spherical, with a relatively uniform size and an average diameter of around 100 nm (Fig. 1A). Ultraviolet–visible (UV–vis) spectra exhibited the characteristic absorption of OSMI-1, indicating its successful encapsulation (Fig. 1B). The encapsulation efficiency of MLH was calculated 93.2 ± 4.2 by using high performance liquid chromatography (HPLC). Dynamic light scattering (DLS) indicated that the diameter of MO@DSSP NPs was approximately 150 nm, with a relatively narrow size distribution (Fig. 1C). The zeta potential was a positive surface charge of +10 mV, further confirming the successful PEGylation and surface modification of MO@DSSP NPs (Fig. 1D). As shown in Fig. S1, the diameter of MO@DSSP NPs showed no obvious change owing to the low GSH level in blood. The PDI and diameter of MO@DSSP NPs showed no significant changes within 48 h under physiological conditions. The release profile revealed that MO@DSSP NPs released the drug in a GSH-dependent manner, as confirmed by high-performance liquid chromatography (HPLC). The release rates of OSMI-1 and MLH significantly increased in a GSH concentration-dependent manner, confirming the redox-responsive ability of MO@DSSP NPs (Fig. 1E and Fig. S2). ROS production was evaluated using 3,3′,5,5′-tetramethylbenzidine (TMB) which was converted into ox-TMB by free radicals, showing a characteristic absorption peak at 650 nm, which confirms the CDT ability of MLH. Fig. 1F shows that MO@DSSP NPs caused a deeper color change of TMB under acid conditions in the presence of Fe^{2+}, as revealed by UV–vis spectra, suggesting the ROS generation ability of MO@DSSP NPs, which was concentration-dependent (Fig. 1G). Furthermore, the analysis of the electron spin resonance (ESR) confirmed the type of free radicals

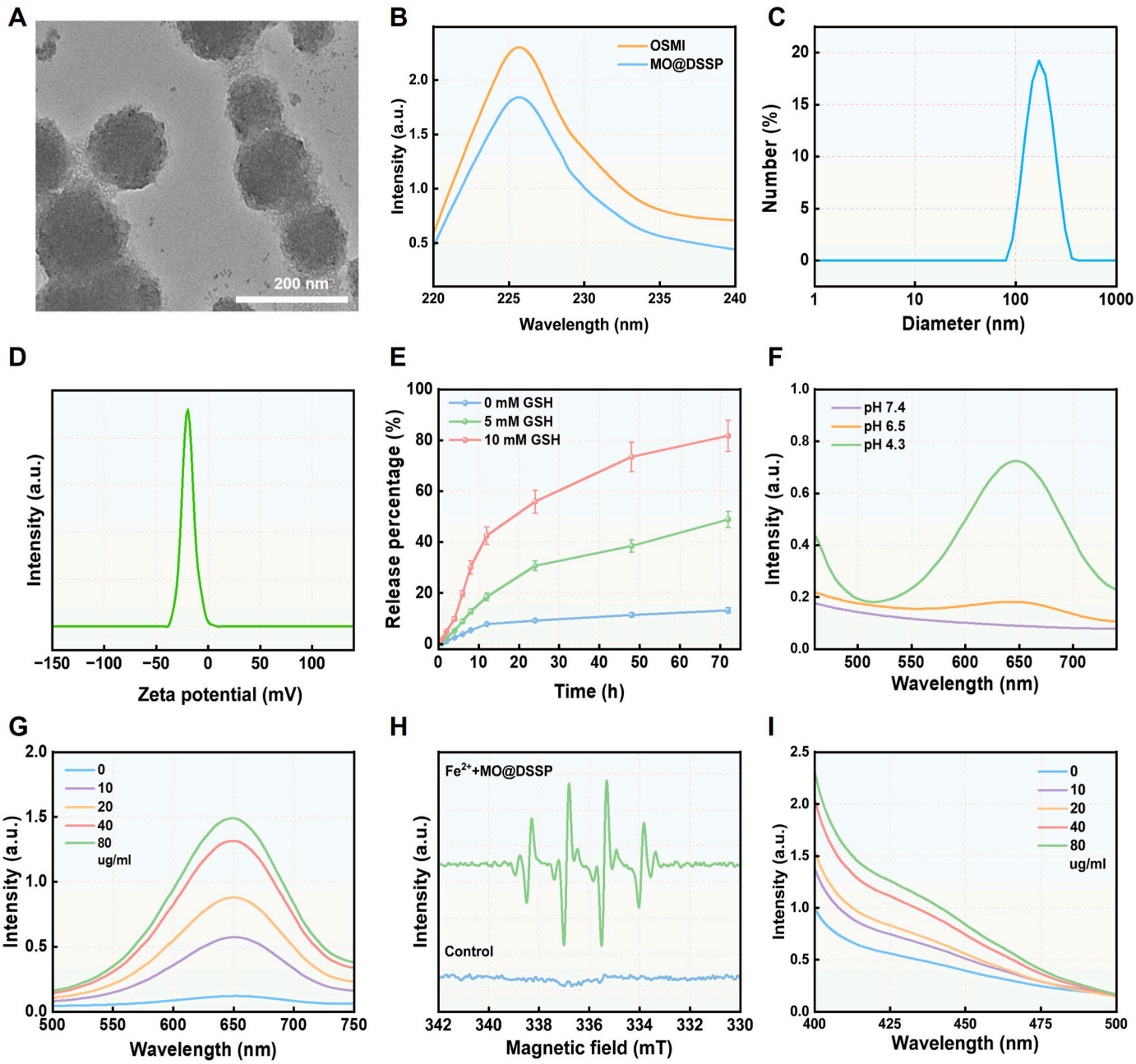

Fig. 1. A) TEM image of MO@DSSP NPs. B) UV–vis spectra of OSMI and MO@ DSSP NPs. C) Diameter and D) zeta potential of MO@ DSSP NPs. E) Cumulative drug release profile of MO@DSSP NPs under different GSH concentrations (n = 3). F) UV–vis spectra of TMB incubated with MO@DSSP NPs in the presence of Fe^{2+} at different pH. G) UV/vis spectra of TMB incubated with MO@DSSP NPs at different concentrations in the presence of Fe^{2+}. H) ESR spectra of •OH trapped by DMPO. I) GSH depletion capacity of MO@DSSP NPs by DTNB assay.

produced by MO@DSSP NPs in the presence of Fe^{2+}, using 5,5-dimethyl-1-pyrroline N-oxide (DMPO) as a spin-trapping agent. A characteristic quartet peak with an intensity ratio of 1:2:2:1 was found (Fig. 1H), indicating that MO@DSSP NPs generated alkoxyl radicals ($^{\bullet}$OR) through Fe^{2+} catalysis. Moreover, the absorbance of MO@DSSP NPs at 412 nm was significantly reduced in a concentration-dependent manner, indicating the potent GSH depletion capacity of MO@DSSP NPs, as revealed by the 5,5′-dithiobis-(2-nitrobenzoic acid) (DTNB) assay (Fig. 1I). Collectively, these findings confirmed that MO@DSSP NPs' ability to generate $^{\bullet}$OR and deplete GSH ensured a self-amplified CDT.

3.2. Therapeutic performance of MO@DSSP NPs on cancer cells

The therapeutic effect of MO@DSSP NPs on the glioma cell line U87MG was evaluated, as shown in Fig. 2. Fig. 2A and B shows a progressive accumulation of the nanoparticles into cancer cells incubated with Cy5-labeled MO@DSSP NPs at different time points, as revealed by the increased fluorescence signal indicating an effective cellular uptake over time. The lysosome tracker and the Cy5-labeled MO@DSSP NPs were colocalized in the lysosomes after 4 h of incubation, suggesting the effective internalization of the nanoparticles, as revealed by confocal laser scanning microscopy (CLSM) images (Fig. 2C and Fig. S3) indicate that this internalization may be potentially involved in the cytotoxic effect. In this experiment, in addition to the Control group and the MO@DSSP group, two distinct groups were also established: M@DSSP and O@DSSP. The M@DSSP group was composed of nanoparticles encapsulating only MLH. The O@DSSP group consisted of nanoparticles encapsulating solely the O-GlcNAcylation inhibitor OSMI-1. MO@DSSP

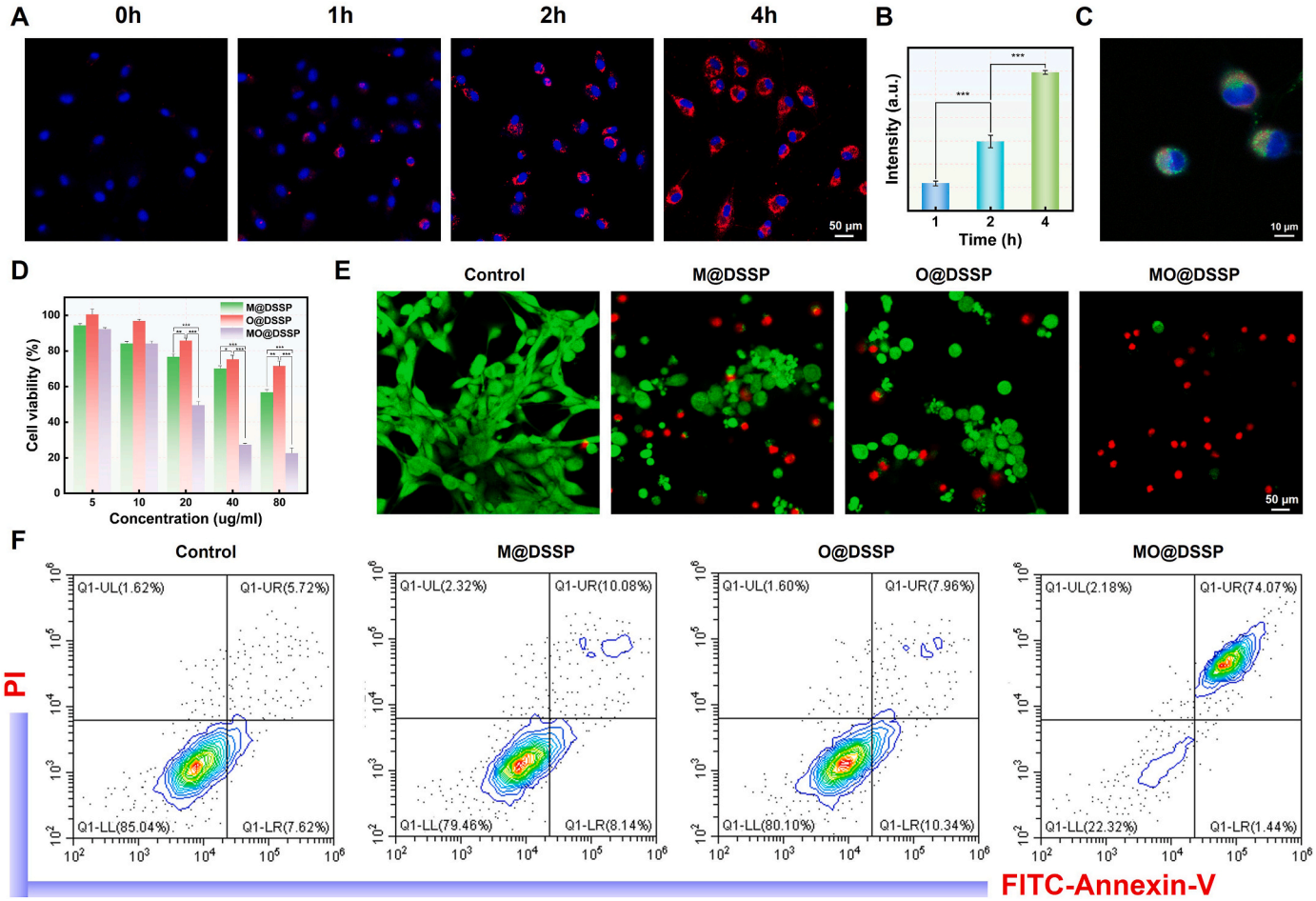

Fig. 2. A) Fluorescence images and B) the corresponding quantification (n = 3) of the fluorescence of U87MG cells treated with Cy5-labeled MO@DSSP NPs at different time points. C) CLSM images showing colocalization of MO@DSSP NPs (red) with lysosome tracker (green) in U87MG cells after 4 h of incubation. D) Cell viability of U87MG cells treated with M@DSSP NPs, O@DSSP NPs, and MO@DSSP NPs (n = 3). E) Live/dead staining of tumor cells following treatment with various formulations. F) Flow cytometry analysis of U87MG cell death under various treatments.

NPs were significantly cytotoxic on U87MG cells, suggesting its potential to inhibit tumor cell viability, as demonstrated by the treatment with different formulations using Cell Counting Kit-8 (CCK8) (Fig. 2D). The CCK-8 results showed that MO@DSSP NPs exhibited no remarkable toxicity to normal cells owing to the low GSH level (Fig. S4). In addition, the qualitative assessment of intracellular H_2O_2 levels in U87MG cells and HT22 cells (used as a normal cell line) using pentafluorobenzenesulfonyl fluorescein as a hydrogen peroxide probe (Fig. S5). The results are consistent with previous literature and further validate the rationale for employing H_2O_2-responsive CDT systems in cancer therapy. To clarify the cell death mechanism, we conducted additional rescue experiments using U87MG cells. Specifically, cells were pretreated with the ferroptosis inhibitor Ferrostatin-1 (Fer-1) or the apoptosis inhibitor Z-VAD-FMK prior to MO@DSSP NPs treatment. Cell viability was then assessed via CCK-8 assay. As shown in Fig. S6, treatment with Fer-1 significantly rescued cell viability after MO@DSSP NPs exposure, while Z-VAD-FMK had minimal effect. These results indicate that ferroptosis, rather than apoptosis, is the dominant mode of cell death induced by MO@DSSP NPs in U87MG cells. Cell viability was further confirmed using the Calce in-AM/PI live/dead co-staining assay (Fig. 2E), which revealed a remarkable increase in the number of dead (red-stained) cells following administration of MO@DSSP NPs compared to the control, indicating an effective tumor cell killing. Finally, a significant increase in U87MG cell death was observed after the treatment with MO@DSSP NPs compared to other groups, as revealed by flow cytometry analysis (Fig. 2F). Furthermore, we conducted additional experiments using Calcein-AM to qualitatively assess the intracellular Fe^{2+} levels in U87MG cells before and after treatment with MO@DSSP NPs. As shown in Fig. S7, a significant enhancement in orange-red fluorescence was observed in the MO@DSSP NPs-treated group, indicating a substantial increase in the labile iron pool within the cells. These results confirm that MO@DSSP NPs effectively promote the release of Fe^{2+} and support their chemodynamic therapeutic activity. This result further supported the potent anti-cancer effects of MO@DSSP NPs on U87MG cells, making it a promising candidate for therapeutic applications.

3.3. *Therapeutic mechanisms of MO@DSSP NPs-Induced cell death*

Our designed nanocarrier system MO@DSSP NPs demonstrated the antitumor effect in vivo, closely associated with the ferroptosis mechanism. After internalization of MO@DSSP NPs by tumor cells, the disulfide bonds undergo cleavage in the reductive environment, depleting GSH and simultaneously releasing OSMI-1 and MLH (Fig. 3A, B and 3C). MO@DSSP NPs in the cells released OSMI-1, which inhibited O-GlcNAcylation (Fig. 3D and S8). This alteration triggered the following cascade of biological responses: the inhibition by OSMI-1 enhanced the binding of FTH to NCOA4, facilitating the transport and degradation of the ferritin complex in lysosomes (Fig. 3E, F and 3H; Fig. S9 and S10). This process disrupted the balance of iron metabolism, leading to an increased release of iron ions from their stable storage in the cell, thereby increasing the levels of the labile iron pool. The expression of

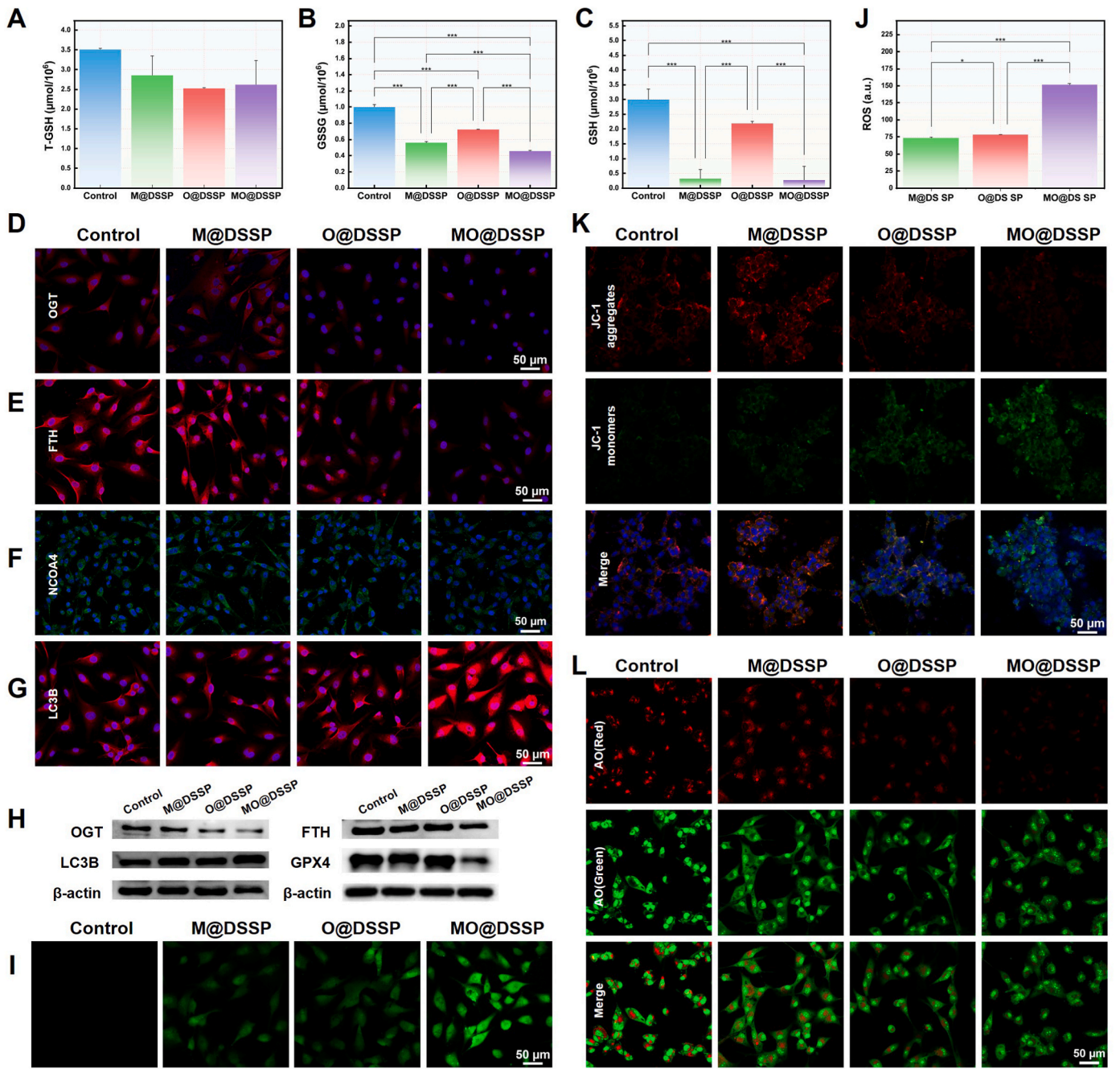

Fig. 3. A) Total glutathione levels (n = 3). B) Oxidized glutathione (GSSG) levels (n = 3). C) GSH levels (n = 3). Expression of D) OGT, E) FTH, F) NCOA4 and G) LC3B by immunofluorescence. H) Western blot analysis of OGT, FTH, LC3B, and GPX4 expression in U87MG cells treated with different formulations. I) CLSM images and J) corresponding quantitative analysis (n = 3) of intracellular ROS levels in U87MG cells under different treatments, detected using the DCFH-DA fluorescent probe. K) CLSM images showing mitochondrial membrane potential in U87MG cells treated with different formulations, assessed by JC-1. L) CLSM images of acridine orange (AO)-stained U87MG cells following incubation with MO@DSSP NPs.

the autophagy-related protein LC3B was significantly upregulated in the MO@DSSP NPs group (Fig. 3G and H and S11), indicating an enhanced autophagic activity. And quantitative data corresponding to Fig. 3D–H can be found in Fig. S12 and S13. This increased autophagy not only promoted the autophagic degradation of ferritin but also facilitated mitophagy. The substantial release of unstable iron ions through autophagy further promoted the Fenton reaction, resulting in the generation of large amounts of ROS (Fig. 3I and J). Their accumulation led to mitochondrial membrane depolarization (Fig. 3K) and lysosomal membrane disruption (Fig. 3L), thereby inducing lipid peroxidation and compromising the integrity of the cell membrane, which are conditions triggering ferroptosis.

The ability of MO@DSSP NPs to induce lipid peroxidation was assessed using the C11-BODIPY probe and the malondialdehyde (MDA) assay kit. The C11-BODIPY assay visually demonstrated an increase in lipid peroxidation in the cells treated with the nanodrug, characterized by a shift from red to green fluorescence and an increase in fluorescence intensity (Fig. 4A). The MDA assay results further corroborated these findings, showing a significant increase in intracellular MDA levels after MO@DSSP NPs treatment (Fig. 4B). Additionally, the remarkable reduction in GPX4 expression suggested the promotion of lipid peroxidation by MO@DSSP NPs and increasing the cellular sensitivity to ferroptosis (Fig. 4C and S14). Overall, our results showed that the nanocarrier system MO@DSSP NPs activated the ferroptosis pathway by

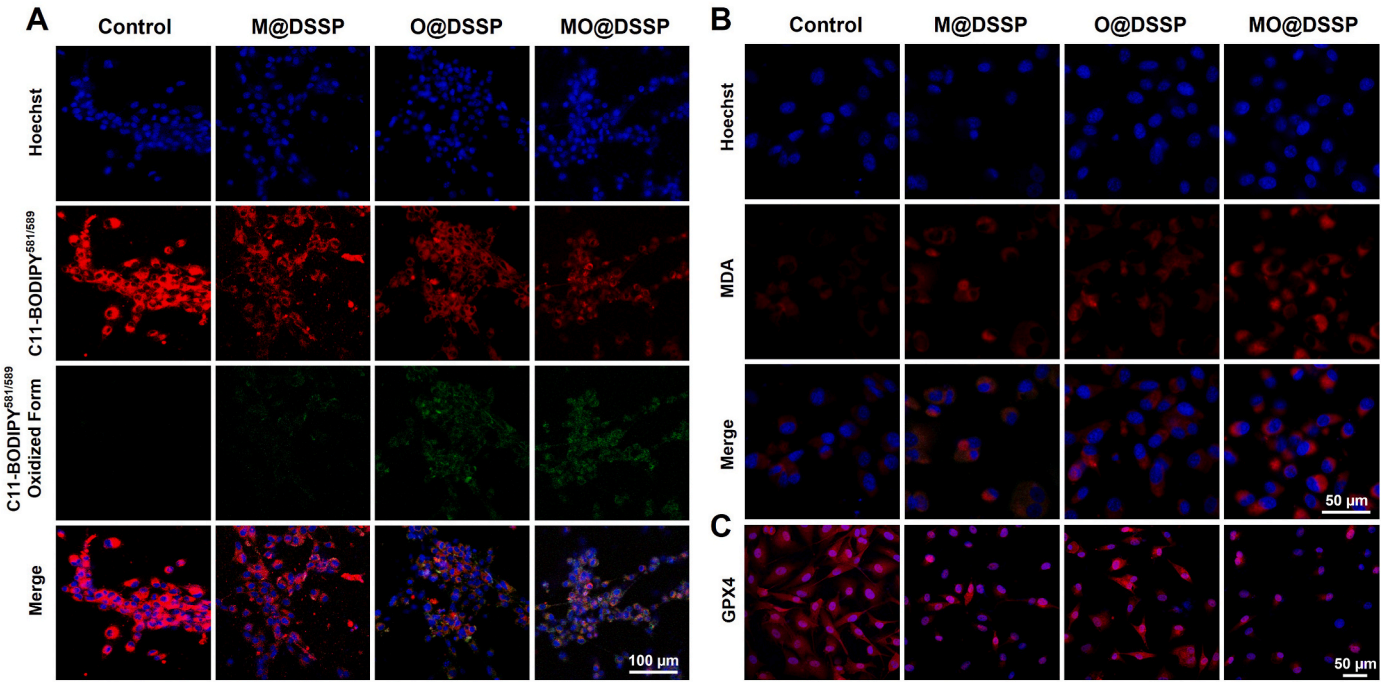

Fig. 4. A) LPO level in U87MG cells treated with different formulations measured by C11-BODIPY581/589 fluorescent probe. B) MDA levels in cancer cells following various formulations. C) Immunofluorescence staining images of GPX4 in tumor cells.

releasing OSMI-1 and MLH, which in turn inhibited O-GlcNAcylation. This modulation regulated the expression and interaction of FTH, NCOA4, and LC3B proteins, thereby effectively exerting its antitumor effects. This mechanism of action provided new perspectives and potential therapeutic targets in cancer treatment.

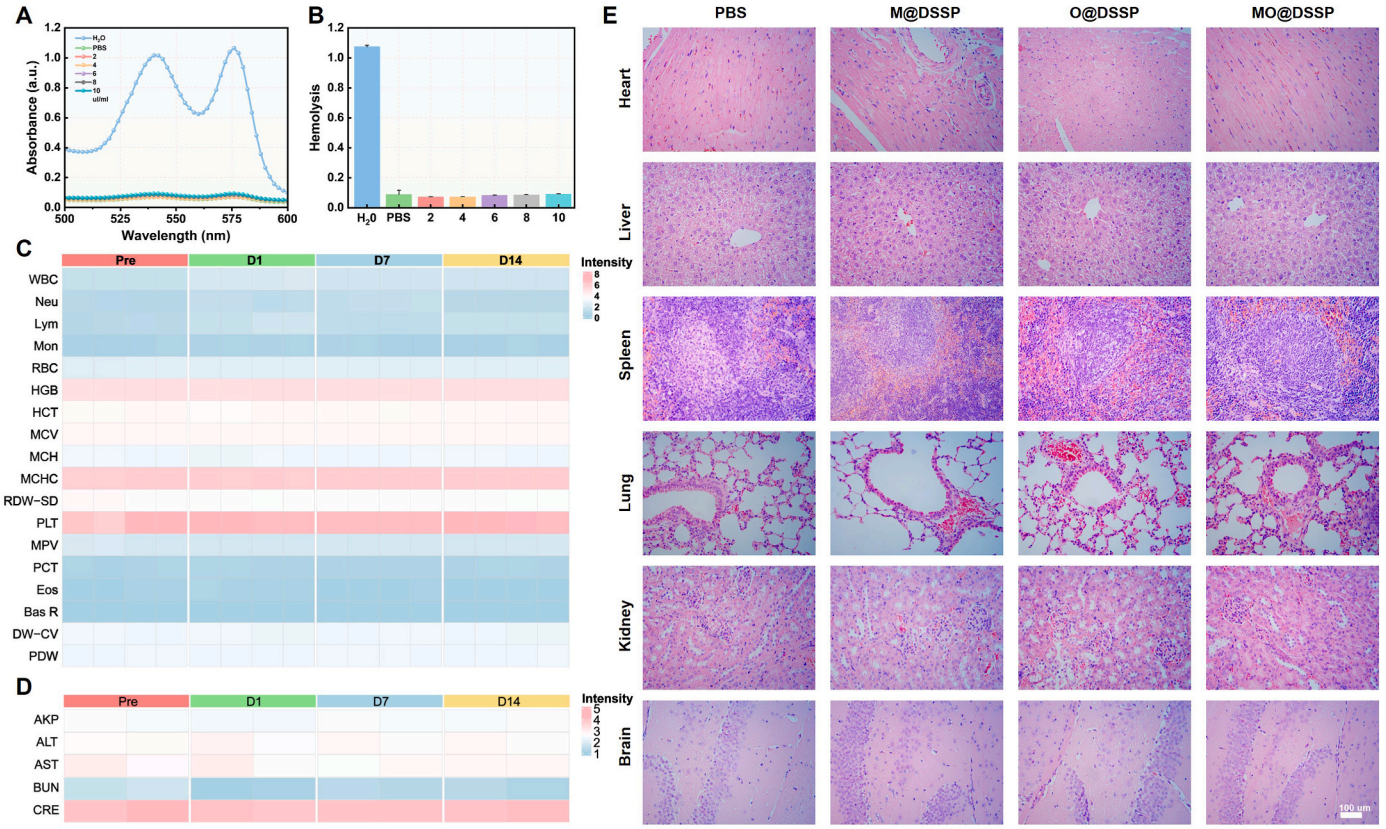

Fig. 5. A) The absorbance spectra and B) hemolysis (n = 3) under different concentrations of MO@DSSP NPs. C) Blood routine examination and D) blood biochemical analysis in mice performed at day 0, 1, 7, and 14 post-injections of MO@DSSP NPs (n = 3). E) Images showing the morphology of the main organs (heart, liver, spleen, lung, kidney and brain) from different treatment groups, harvested 14 days after treatment and stained by H&E.

3.4. In vivo biosafety of MO@DSSP NPs

The biosafety of MO@DSSP NPs was assessed before the evaluation of their therapeutic effect in mice. These findings revealed that MO@DSSP NPs induced a minimal hemolytic activity (<5 %) in mice over a concentration range of 0–10 μL/mL, indicating the feasibility of nanoparticles (Fig. 5A and B). All animal experimental protocols were approved in advance by the Ethics Committee of Fujian Medical University. Blood routine examination and biochemical analyses indicated that the treatment with MO@DSSP did not induce any significant change in blood parameters (Fig. 5C and D, S15, and S16). Consistently, the histological examination of the main organs by hematoxylin and eosin (H&E) staining 14 days post-injection did not reveal any detectable sign of tissue damage or abnormality in the MO@DSSP group, highlighting its excellent biocompatibility (Fig. 5E).

3.5. In vivo antitumor effect of MO@DSSP NPs

The in vivo distribution of MO@DSSP NPs was assessed using live animal imaging. Cy5-labeled MO@DSSP NPs preferentially accumulated at the tumor site in U87MG-bearing nude mice compared to mice injected with Cy5 alone, as revealed by fluorescence imaging (Fig. 6A, left panel). This indicated the excellent targeting ability and sustained tumor accumulation of MO@DSSP NPs, suggesting their potential for long-lasting therapeutic effects and precise targeting within tumor tissues. The tumor volume trend over time showed a rapid increase in the PBS-treated group, while it significantly decreased in the MO@DSSP group, emphasizing the strong inhibitory effect of MO@DSSP NPs on tumor growth (Fig. 6B). The experimental results show that 24 h after the injection of MO@DSSP NPs, the MO@DSSP NPs are mainly enriched in the tumors (Fig. S17). Endpoint tumor weight measurements further corroborated these findings, showing that tumors in the PBS group weighed more than those in the M@DSSP and O@DSSP groups. Notably,

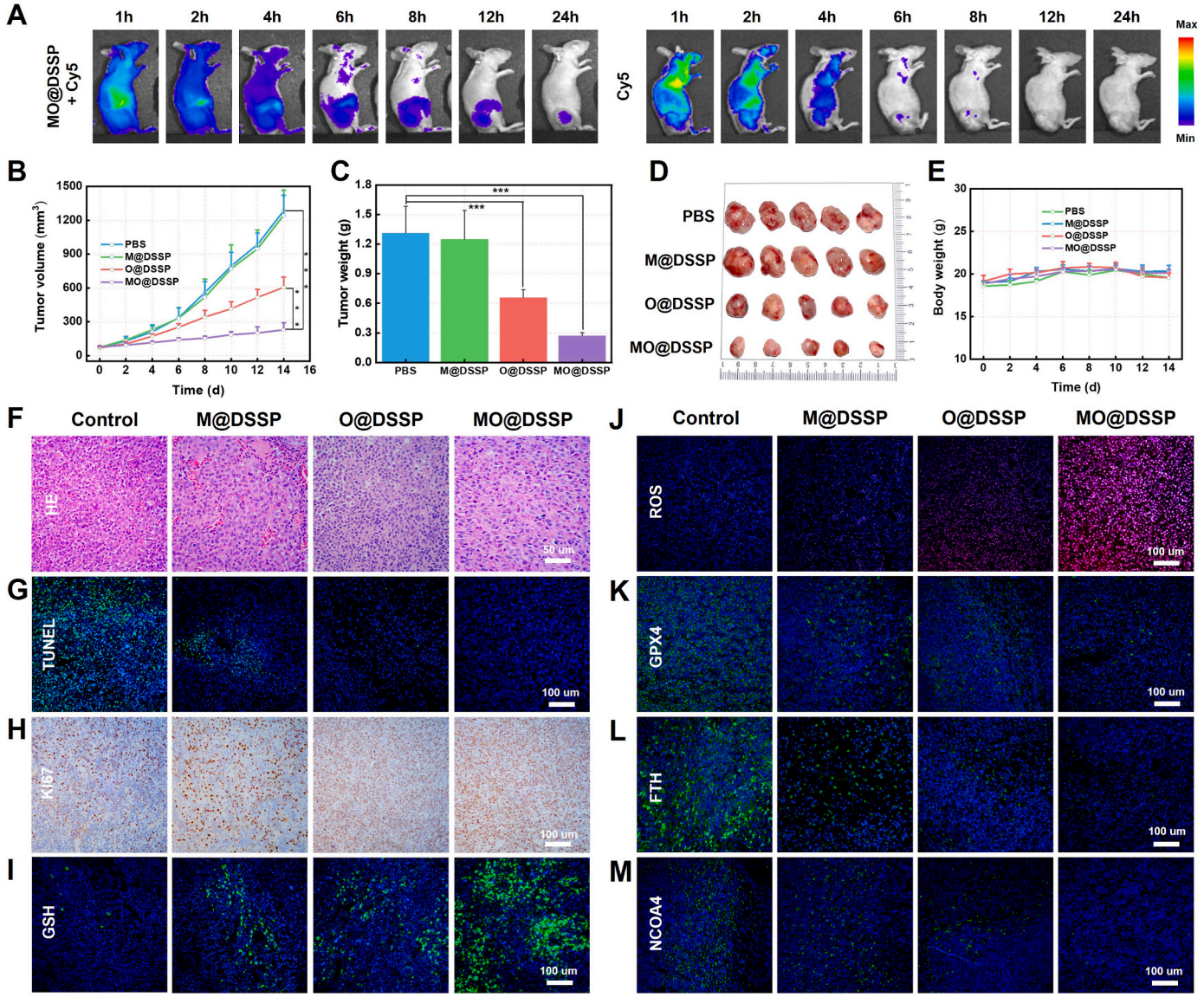

Fig. 6. A) Fluorescence imaging demonstrating biodistribution of MO@DSSP in tumor-bearing mice at various time points (left panel), as well as that of free Cy5 in tumor-bearing mice at the same time points (right panel). B) Tumor growth curves following with various formulations (n = 5), ***$p < 0.001$. C) Average weight and D) image of tumors harvested from different groups, ***$p < 0.001$. E) Body weight of mice during the treatment period. F) H&E and G) TUNEL staining of tumors collected from different groups. H) Immunohistochemical (IHC) staining shows the expression of Ki67 in different treatment groups. I) Fluorescence staining of GSH in tumor tissues of each group. J) Detection of ROS levels in tumor tissues of each group by fluorescence staining. Immunofluorescence analysis showing the expression of K) GPX4, L) FTH and M) NCOA4.

the MO@DSSP group showed the lowest tumor weight (Fig. 6C, $P < 0.001$), further confirming the superior antitumor activity of MO@DSSP NPs. Fig. 6D shows the tumor size of different treatment groups, with MO@DSSP NPs exerting the most potent antitumor effect. Throughout the treatment period, no noticeable alterations in body weight were detected in any of the groups. (Fig. 6E), indicating that MO@DSSP NPs exerted their robust antitumor effects without compromising the biological safety.

Further confirmation of the antitumor effect of MO@DSSP NPs was obtained by H&E staining, TUNEL staining, and Ki-67 immunostaining. A remarkable damage to cancer cells was observed in the MO@DSSP group by H&E, characterized by cytoplasmic vacuolization and cell necrosis (Fig. 6F). The MO@DSSP NPs-treated tumors showed the highest amount of apoptosis, as revealed by the TUNEL assay (Fig. 6G), further confirming the therapeutic effect. Additionally, a marked reduction in tumor cell proliferation was found by Ki-67 staining (Fig. 6H), underscoring the potential of MO@DSSP NPs as an effective chemodynamic therapeutic agent. Immunohistochemistry analysis of GSH, ROS, GPX4, FTH, and NCOA4 protein expression in the tumors provided further evidence of the induction of MO@DSSP NPs-mediated ferroptosis. A significant decrease in GSH levels (Fig. 6I), inhibition of GPX4 expression (Fig. 6J), and reduced expression of both FTH and NCOA4 (Fig. 6K and L) were found. These findings supported the antitumor effects of CDT-mediated ferroptosis, highlighting the potential of MO@DSSP NPs as a promising CDT for an effective and safe cancer treatment.

4. Conclusions

This study describes a new and efficient approach for enhancing CDT with a significant antitumor effect and high safety profile. The synthesized MO@DSSP NPs show an exceptional catalytic performance, enabling the specific targeting of tumors and GSH-responsive drug release. MO@DSSP NPs promote ferritinophagy and mitophagy by inhibiting O-GlcNAcylation, resulting in the release of free iron through autophagy. This substantial increase in the endogenous LIP facilitates the in-situ initiation of the Fenton reaction, generating ·OH that further induces LPO and inactivate GPX4, thereby triggering ferroptosis in tumor cells and promoting tumor ablation. Overall, this research demonstrates a CDT strategy through multifunctional nanoparticles designed to enhance endogenous LIP, significantly increasing tumor cell sensitivity to ferroptosis while minimizing the damage to healthy tissues. These findings provide valuable insights into the development of advanced nanomaterials in cancer therapy, offering promising potential to improve future tumor treatment strategies.

CRediT authorship contribution statement

Penghui Wei: Writing – review & editing, Writing – original draft, Formal analysis, Data curation, Conceptualization. **Xuegang Niu:** Formal analysis, Data curation. **Dengliang Wang:** Formal analysis. **Chengzhong Du:** Investigation. **Mingtao Zhu:** Methodology. **Hongjia Zheng:** Methodology. **Yongrui Hu:** Resources. **Yu Tian:** Software. **Wei Huang:** Software. **Chengyu Ding:** Validation. **Yuanxiang Lin:** Supervision. **Yang Zhu:** Writing – review & editing, Writing – original draft, Supervision, Funding acquisition. **Dezhi Kang:** Supervision.

Funding declaration

This work was supported by the Joint Funds for the innovation of Science and Technology, Fujian province (Grant number: 2023Y9090, 2024Y9163), Fujian Medical Innovation Project Funding Program (2024CXA017). The “Double high” Construction Project of Neurosurgery Department of Fujian Medical Center for Neurological Diseases (2023YSJYX-YJS-3)

Declaration of competing interest

The authors declared that they have no known competing financial interests or personal relationships that could have appeared to influence the work reported in this paper.

Appendix A. Supplementary data

Supplementary data to this article can be found online at https://doi.org/10.1016/j.mtbio.2025.101913.

Data availability

Data will be made available on request.

References

[1] X. Niu, Y. Zhu, C. Ding, J. Ma, P. Wei, Y. Lin, W. Fang, Q. He, C. Li, J. Cheng, J. Zou, L. Lin, X. Chen, D. Kang, Dual-active center AgFeCu nanocatalyst for tumor destruction via self-catalytically enhanced mild photothermal therapy, Adv. Funct. Mater. (2023) 2306778.
[2] Y. Zhu, P. Gong, J. Wang, J. Cheng, W. Wang, H. Cai, R. Ao, H. Huang, M. Yu, L. Lin, X. Chen, Amplification of lipid peroxidation by regulating cell membrane unsaturation to enhance chemodynamic therapy, Angew. Chem., Int. Ed. 62 (12) (2023) e202218407.
[3] P. Zhao, H. Li, W. Bu, A forward vision for chemodynamic therapy: issues and opportunities, Angew. Chem. Int. Ed. 62 (7) (2023) e202210415.
[4] D. Jana, Y. Zhao, Strategies for enhancing cancer chemodynamic therapy performance, Explorations 2 (2) (2022) 20210238.
[5] Z. Tang, Y. Liu, M. He, W. Bu, Chemodynamic therapy: tumour microenvironment-mediated Fenton and fenton-like reactions, Angew. Chem. Int. Ed. 58 (4) (2019) 946–956.
[6] K. Zheng, R. Song, R. Li, M. Liu, Y. Ba, W. Jiang, K. Fan, Nanomaterials for refining tumor microenvironment and enhancing therapy in head and neck squamous cell carcinoma: a review, Oncol. Trans. Med. 10 (4) (2024).
[7] L.-S. Lin, T. Huang, J. Song, X.-Y. Ou, Z. Wang, H. Deng, R. Tian, Y. Liu, J.-F. Wang, Y. Liu, G. Yu, Z. Zhou, S. Wang, G. Niu, H.-H. Yang, X. Chen, Synthesis of copper peroxide nanodots for H2O2 self-supplying chemodynamic therapy, J. Am. Chem. Soc. 141 (25) (2019) 9937–9945.
[8] Y. Zhu, C. Ding, W. Fang, T. Li, L. Yan, Y. Tian, W. Huang, P. Wei, J. Ma, X. Lin, W. Huang, Y. Lin, J. Zou, X. Chen, Metal-polyphenol self-assembled nanodots for NIR-II fluorescence imaging-guided chemodynamic/photodynamic therapy-amplified ferroptosis, Acta Biomater. 185 (2024) 361–370.
[9] Y. Zhu, X. Niu, T. Wu, J. Cheng, J. Zou, Y. Pan, Y. Tian, W. Huang, C. Ding, Y. Lin, D. Kang, X. Chen, Metal-phenolic nanocatalyst rewires metabolic vulnerability for catalytically amplified ferroptosis, Chem. Eng. J. (Amsterdam, Neth.) 485 (2024) 150126.
[10] S. Gao, Y. Jin, K. Ge, Z. Li, H. Liu, X. Dai, Y. Zhang, S. Chen, X. Liang, J. Zhang, Self-supply of O2 and H2O2 by a nanocatalytic medicine to enhance combined chemo/chemodynamic therapy, Adv. Sci. 6 (24) (2019) 1902137.
[11] Y. Zhou, S. Fan, L. Feng, X. Huang, X. Chen, Manipulating intratumoral Fenton chemistry for enhanced chemodynamic and chemodynamic-synergized multimodal therapy, Adv. Mater. 33 (48) (2021) 2104223.
[12] J. Lu, Y. Yang, Q. Xu, Y. Lin, S. Feng, Y. Mao, D. Wang, S. Wang, Q. Zhao, Recent advances in multi-configurable nanomaterials for improved chemodynamic therapy, Coord. Chem. Rev. 474 (2023) 214861.
[13] X. Wang, X. Zhong, Z. Liu, L. Cheng, Recent progress of chemodynamic therapy-induced combination cancer therapy, Nano Today 35 (2020) 100946.
[14] S. Wang, Z. Wang, G. Yu, Z. Zhou, O. Jacobson, Y. Liu, Y. Ma, F. Zhang, Z.-Y. Chen, X. Chen, Tumor-specific drug release and reactive oxygen species generation for cancer chemo/chemodynamic combination therapy, Adv. Sci. 6 (5) (2019) 1801986.
[15] M. Yu, Z. Ye, S. Liu, Y. Zhu, X. Niu, J. Wang, R. Ao, H. Huang, H. Cai, Y. Liu, X. Chen, L. Lin, Redox-active ferrocene quencher-based supramolecular nanomedicine for NIR-II fluorescence-monitored chemodynamic therapy, Angew. Chem. Int. Ed. 63 (10) (2024) e202318155.
[16] G. Guo, H. Zhang, H. Shen, C. Zhu, R. He, J. Tang, Y. Wang, X. Jiang, J. Wang, W. Bu, X. Zhang, Space-selective chemodynamic therapy of CuFe5O8 nanocubes for implant-related infections, ACS Nano 14 (10) (2020) 13391–13405.
[17] J. Xin, C. Deng, O. Aras, M. Zhou, C. Wu, F. An, Chemodynamic nanomaterials for cancer theranostics, J. Nanobiotechnol. 19 (1) (2021) 192.
[18] L. Lin, S. Wang, H. Deng, W. Yang, L. Rao, R. Tian, Y. Liu, G. Yu, Z. Zhou, J. Song, H.-H. Yang, Z.-Y. Chen, X. Chen, Endogenous labile iron pool-mediated free radical generation for cancer chemodynamic therapy, J. Am. Chem. Soc. 142 (36) (2020) 15320–15330.
[19] Y. Huang, S. Wu, L. Zhang, Q. Deng, J. Ren, X. Qu, A metabolic multistage glutathione depletion used for tumor-specific chemodynamic therapy, ACS Nano 16 (3) (2022) 4228–4238.
[20] Y. Sang, F. Cao, W. Li, L. Zhang, Y. You, Q. Deng, K. Dong, J. Ren, X. Qu, Bioinspired construction of a nanozyme-based H2O2 homeostasis disruptor for intensive chemodynamic therapy, J. Am. Chem. Soc. 142 (11) (2020) 5177–5183.

[21] Z. Wang, J. Yang, G. Qin, C. Zhao, J. Ren, X. Qu, An intelligent nanomachine guided by DNAzyme logic system for precise chemodynamic therapy, Angew. Chem. Int. Ed. 61 (38) (2022) e202204291.
[22] Y. Zhu, D. Wang, C. Du, T. Wu, P. Wei, H. Zheng, G. Li, S. Zheng, L. Su, L. Yan, Y. Hu, H. Wang, L. Lin, C. Ding, X. Chen, Ruthenium single-atom nanozyme driven sonosensitizer with oxygen vacancies enhances electron–hole separation efficacy and remodels tumor microenvironment for sonodynamic-amplified ferroptosis, Adv. Sci. (2025) 2416997.
[23] T. Wu, P. Wei, P. Zhao, X. Niu, C. Ding, Y. Zhu, Engineering local coordination environment of manganese single-atom enzyme for amplified infected wound therapy, Chem. Eng. J. (Amsterdam, Neth.) 514 (2025) 163247.
[24] P.P. Mueller, T. May, A. Perz, H. Hauser, M. Peuster, Control of smooth muscle cell proliferation by ferrous iron, Biomaterials 27 (10) (2006) 2193–2200.
[25] S. Puig, L. Ramos-Alonso, A.M. Romero, M.T. Martínez-Pastor, The elemental role of iron in DNA synthesis and repair, Metallomics 9 (11) (2017) 1483–1500.
[26] C. Yi, G. Jia, G. Hou, Q. Dai, W. Zhang, G. Zheng, X. Jian, C.-G. Yang, Q. Cui, C. He, Iron-catalysed oxidation intermediates captured in a DNA repair dioxygenase, Nature 468 (7321) (2010) 330–333.
[27] J. Kaplan, D.M. Ward, The essential nature of iron usage and regulation, Curr. Biol. 23 (15) (2013) R642–R646.
[28] O. Kakhlon, Z.I. Cabantchik, The labile iron pool: characterization, measurement, and participation in cellular processes1 1This article is part of a series of reviews on "Iron and Cellular Redox Status." the full list of papers may be found on the homepage of the journal, Free Radical Biol. Med. 33 (8) (2002) 1037–1046.
[29] R.C. Hider, X.L. Kong, Glutathione: a key component of the cytoplasmic labile iron pool, BioMetals (Oxf.) 24 (6) (2011) 1179–1187.
[30] A.M. Konijn, H. Glickstein, B. Vaisman, E.G. Meyron-Holtz, I.N. Slotki, Z. I. Cabantchik, The cellular labile iron pool and intracellular ferritin in K562 cells, Blood 94 (6) (1999) 2128–2134.
[31] H. Glickstein, R. Ben El, M. Shvartsman, Z.I. Cabantchik, Intracellular labile iron pools as direct targets of iron chelators: a fluorescence study of chelator action in living cells, Blood 106 (9) (2005) 3242–3250.
[32] H.N. Brawley, A.C. Kreinbrink, J.D. Hierholzer, S.W. Vali, P.A. Lindahl, Labile iron pool of isolated Escherichia coli cytosol likely includes Fe-ATP and Fe-citrate but not Fe-glutathione or aqueous Fe, J. Am. Chem. Soc. 145 (4) (2023) 2104–2117.
[33] P. Arosio, S. Levi, Ferritin, iron homeostasis, and oxidative damage1, 2 1Guest Editor: mario Comporti 2This article is part of a series of reviews on "Iron and Cellular Redox Status." the full list of papers may be found on the homepage of the journal, Free Radical Biol. Med. 33 (4) (2002) 457–463.
[34] D.W. Reif, Ferritin as a source of iron for oxidative damage, Free Radical Biol. Med. 12 (5) (1992) 417–427.
[35] S. Granick, Ferritin: its properties and significance for iron metabolism, Chem. Rev. 38 (3) (1946) 379–403.
[36] J. Wang, H. Ding, Y. Zhu, Y. Liu, M. Yu, H. Cai, R. Ao, H. Huang, P. Gong, Y. Liao, Z. Chen, L. Lin, X. Chen, H. Yang, Iron-siRNA nanohybrids for enhanced chemodynamic therapy via ferritin heavy chain downregulation, Angew. Chem. Int. Ed. 62 (22) (2023) e202302255.
[37] E. Park, S.W. Chung, ROS-mediated autophagy increases intracellular iron levels and ferroptosis by ferritin and transferrin receptor regulation, Cell Death Dis. 10 (11) (2019) 822.
[38] K.-H. Zhang, H.-Y. Tian, X. Gao, W.-W. Lei, Y. Hu, D.-M. Wang, X.-C. Pan, M.-L. Yu, G.-J. Xu, F.-K. Zhao, J.-G. Song, Ferritin heavy chain–mediated iron homeostasis and subsequent increased reactive oxygen species production are essential for epithelial-mesenchymal transition, Cancer Res. 69 (13) (2009) 5340–5348.
[39] C.G. Pham, C. Bubici, F. Zazzeroni, S. Papa, J. Jones, K. Alvarez, S. Jayawardena, E. De Smaele, R. Cong, C. Beaumont, F.M. Torti, S.V. Torti, G. Franzoso, Ferritin heavy chain upregulation by NF-κB inhibits TNFα-induced apoptosis by suppressing reactive oxygen species, Cell 119 (4) (2004) 529–542.
[40] C. Mukherjee, T. Kling, B. Russo, K. Miebach, E. Kess, M. Schifferer, L.D. Pedro, U. Weikert, M.K. Fard, N. Kannaiyan, M. Rossner, M.-L. Aicher, S. Goebbels, K.-A. Nave, E.-M. Krämer-Albers, A. Schneider, M. Simons, Oligodendrocytes provide antioxidant defense function for neurons by secreting ferritin heavy chain, Cell Metab. 32 (2) (2020) 259–272.e10.
[41] F. Yu, Q. Zhang, H. Liu, J. Liu, S. Yang, X. Luo, W. Liu, H. Zheng, Q. Liu, Y. Cui, G. Chen, Y. Li, X. Huang, X. Yan, J. Zhou, Q. Chen, Dynamic O-GlcNAcylation coordinates ferritinophagy and mitophagy to activate ferroptosis, Cell Discov 8 (1) (2022) 40.
[42] J. Dixon Scott, Kathryn M. Lemberg, Michael R. Lamprecht, R. Skouta, Eleina M. Zaitsev, Caroline E. Gleason, Darpan N. Patel, Andras J. Bauer, Alexandra M. Cantley, Wan S. Yang, B. Morrison III, R. Brent, Stockwell, ferroptosis: an iron-dependent form of nonapoptotic cell death, Cell 149 (5) (2012) 1060–1072.
[43] J.P. Friedmann Angeli, M. Schneider, B. Proneth, Y.Y. Tyurina, V.A. Tyurin, V. J. Hammond, N. Herbach, M. Aichler, A. Walch, E. Eggenhofer, D. Basavarajappa, O. Rådmark, S. Kobayashi, T. Seibt, H. Beck, F. Neff, I. Esposito, R. Wanke, H. Förster, O. Yefremova, M. Heinrichmeyer, G.W. Bornkamm, E.K. Geissler, S. B. Thomas, B.R. Stockwell, V.B. O'Donnell, V.E. Kagan, J.A. Schick, M. Conrad, Inactivation of the ferroptosis regulator Gpx4 triggers acute renal failure in mice, Nat. Cell Biol. 16 (12) (2014) 1180–1191.
[44] Wan S. Yang, R. SriRamaratnam, Matthew E. Welsch, K. Shimada, R. Skouta, Vasanthi S. Viswanathan, Jaime H. Cheah, Paul A. Clemons, Alykhan F. Shamji, Clary B. Clish, Lewis M. Brown, Albert W. Girotti, Virginia W. Cornish, Stuart L. Schreiber, Brent R. Stockwell, Regulation of ferroptotic cancer cell death by GPX4, Cell 156 (1) (2014) 317–331.
[45] G. Zhu, A. Murshed, H. Li, J. Ma, N. Zhen, M. Ding, J. Zhu, S. Mao, X. Tang, L. Liu, F. Sun, L. Jin, Q. Pan, O-GlcNAcylation enhances sensitivity to RSL3-induced ferroptosis via the YAP/TFRC pathway in liver cancer, Cell Death Discov. 7 (1) (2021) 83.
[46] J. Tang, G. Long, K. Hu, D. Xiao, S. Liu, L. Xiao, L. Zhou, Y. Tao, Targeting USP8 inhibits O-GlcNAcylation of SLC7A11 to promote ferroptosis of hepatocellular carcinoma via stabilization of OGT, Adv. Sci. 10 (33) (2023) 2302953.